

Figure 2 Time evolution of the protostellar wobble, given as the radial displacement r from the centre of mass of the system. The protostellar wobble grows roughly exponentially in time as the spiral arms grow in amplitude. After ~ 500 yr, two GGPPs form, and the amplitude of the wobble is modulated by beating between the orbital frequencies of the two GGPPs. A second model, which differed only in having additional $m = 2, 3$ and 4 initial density perturbations, behaved very similarly. (See text for details of m .)

equation for the disk's gravitational potential.

The growth of $m = 1$ modes typically results in a shift in the centre of mass of the disk away from its geometric centre. The central protostar then responds in this model by shifting in the opposite direction by an amount sufficient to preserve the exact location of the centre of mass of the system. The shifting position of the central protostar then feeds back to the disk through the star's gravitational acceleration.

Figure 1 shows the time evolution of the location of the protostar with respect to the centre of mass of the system. The protostar's wobble increases dramatically as the spiral arms grow in amplitude and form two GGPPs with masses of $\sim 0.01 M_{\odot}$, orbiting at ~ 5 AU and ~ 10 AU. The protostar's displacement from the centre of mass is minimized when the GGPPs are aligned on opposite sides of the protostar and maximized when they are on the same side (Fig. 1b). The non-axisymmetric distribution of the remainder of the disk also contributes significantly to the total protostellar wobble.

Figure 2 shows that following an initial phase of approximately exponential growth of the $m = 1$ perturbation, the mode saturates at a level that results in a protostellar wobble with an amplitude of ~ 0.1 AU. This wobble is modulated by beating between the orbital frequencies of the two GGPPs (with periods of ~ 9 yr and ~ 18 yr), yielding a period of ~ 18 yr.

The masses of the giant planets eventually formed by these $\sim 0.01 M_{\odot}$ GGPPs are uncertain, as considerable evolution remains before reaching planetary densities. In addition, future disk evolution models may well show that GGPPs can form in less-massive disks, leading to lower-mass GGPPs and smaller protostellar wobbles. Nevertheless, the model suggests that GGPP formation can lead to astrometric wobbles of the order of 0.1 AU in solar-mass YSOs. At a distance of 140 pc (for example, the Taurus star-forming region), this corresponds to an angular displacement of ~ 0.7 milliarcsec (0.7 mas), measurable with the precision of 0.1 mas per night attained by G. Gatewood's astrometric photometer at the Keck Observatory²¹.

The growth of spiral arms before GGPP formation would produce a signal about 10 times smaller (Fig. 2), ~ 70 microarcsec (70 μ as). This signal would be readily detectable by the Keck Interferometer²² or by the Space Interferometry Mission²³, which are expected to have astrometric accuracies close to ~ 10 μ as and ~ 1 μ as, respectively. However, detecting the growth of spiral arms would require fortuitous timing, because of the brief duration of

this phase, requiring the observation of an even larger ensemble of young stars.

Searching for evidence of GGPP formation around YSOs would provide a critical test of our understanding of giant-planet formation, and should clarify the relationship between giant planets and circumstellar disks, as well as any brown-dwarf protostars that would also be discovered by such a search. \square

Received 24 November 1997; accepted 3 March 1998.

1. Gatewood, G. Lalande 21185. *Bull. Am. Astron. Soc.* **28**, 885 (1996).
2. Mayor, M. & Queloz, D. A Jupiter-mass companion to a solar-type star. *Nature* **378**, 355–359 (1995).
3. Butler, R. P. & Marcy, G. W. A planet orbiting 47 Ursae Majoris. *Astrophys. J.* **464**, L153–L156 (1996).
4. Butler, R. P., Marcy, G. W., Williams, E., Hauser, H. & Shirts, P. Three new "51 Pegasi-Type" planets. *Astrophys. J.* **474**, L115–L118 (1997).
5. Cochran, W. D., Hatzes, A. P., Butler, R. P. & Marcy, G. W. The discovery of a planetary companion to 16 Cygni B. *Astrophys. J.* **483**, 457–463 (1997).
6. Noyes, R. W. *et al.* A planet orbiting the star Rho Coronae Borealis. *Astrophys. J.* **483**, L111–L114 (1997).
7. Kuiper, G. P. On the origin of the solar system. *Proc. Natl Acad. Sci. USA* **37**, 1–14 (1951).
8. Boss, A. P. Giant planet formation by gravitational instability. *Science* **276**, 1836–1839 (1997).
9. Pollack, J. B. Origin and history of the outer planets: theoretical models and observational constraints. *Annu. Rev. Astron. Astrophys.* **22**, 389–424 (1984).
10. Lissauer, J. J. Timescales for planetary accretion and the structure of the protoplanetary disk. *Icarus* **69**, 249–265 (1987).
11. Wetherill, G. W. Formation of the Earth. *Annu. Rev. Earth Planet. Sci.* **18**, 205–256 (1990).
12. Pollack, J. B. *et al.* Formation of the giant planets by concurrent accretion of solids and gas. *Icarus* **124**, 62–85 (1996).
13. Adams, F. C., Ruden, S. P. & Shu, F. H. Eccentric gravitational instabilities in nearly Keplerian disks. *Astrophys. J.* **347**, 959–975 (1989).
14. Laughlin, G. & Bodenheimer, P. Nonaxisymmetric evolution in protostellar disks. *Astrophys. J.* **436**, 335–354 (1994).
15. Trilling, D. *et al.* Orbital evolution and migration of giant planets: modeling extrasolar planets. *Astrophys. J.* (in the press).
16. Gatewood, G. On the astrometric detection of neighboring planetary systems. *Icarus* **27**, 1–12 (1976).
17. Beckwith, S. V. W., Sargent, A. I., Chini, R. S. & Güsten, R. A survey for circumstellar disks around young stellar objects. *Astron. J.* **99**, 924–945 (1990).
18. Boss, A. P. & Myhill, E. A. Protostellar hydrodynamics: constructing and testing a spatially and temporally second-order accurate method. I. Spherical coordinates. *Astrophys. J. Suppl. Ser.* **83**, 311–327 (1992).
19. Boss, A. P. Evolution of the solar nebula. III. Protoplanetary disks undergoing mass accretion. *Astrophys. J.* **469**, 906–920 (1996).
20. Toomre, A. On the gravitational stability of a disk of stars. *Astrophys. J.* **139**, 1217–1238 (1964).
21. Snyder Hale, A., Gatewood, G. D., Hale, D. D. S., Persinger, W. T. & McMillan, R. S. The multichannel astrometric photometer with spectrograph: A new instrument for the characterization of extrasolar planetary systems. *Lunar Planet. Sci. Conf. XXVIII*, 1359–1360 (1997).
22. Swanson, P. *Keck Interferometer Implementation Plan* (Jet Propulsion Lab., Pasadena, 1997).
23. Allen, R. J., Peterson, D. & Shao, M. *Proc. SPIE* **2871**, 504–515 (1997).

Acknowledgements. I thank D. Spergel for prompting this investigation through a cogent question, and J. Graham for improvements to the manuscript. The calculations were performed on the DEC Alpha workstations of the Carnegie Institution of Washington. This research was partially supported by NASA's Planetary Geology and Geophysics Program.

Correspondence and requests for materials should be addressed to the author (e-mail: boss@dtm.ciw.edu).

Experimental realization of a quantum algorithm

Isaac L. Chuang^{*}, Lieven M. K. Vandersypen[†], Xinlan Zhou[†], Debbie W. Leung[‡] & Seth Lloyd[§]

^{*} IBM Almaden Research Center, San Jose, California 95120, USA

[†] Solid State and Photonics Laboratory, Stanford University, Stanford, California 94305, USA

[‡] Edward L. Ginzton Laboratory, Stanford University, Stanford, California 94305, USA

[§] MIT Department of Mechanical Engineering, Cambridge, Massachusetts 02139, USA

Quantum computers^{1–5} can in principle exploit quantum-mechanical effects to perform computations (such as factoring large numbers or searching an unsorted database) more rapidly than classical computers^{1,2,6–8}. But noise, loss of coherence, and manufacturing problems make constructing large-scale quantum computers difficult^{9–13}. Although ion traps and optical cavities offer promising experimental approaches^{14,15}, no quantum algorithm has yet been implemented with these systems. Here we

report the experimental realization of a quantum algorithm using a bulk nuclear magnetic resonance technique^{16–18}, in which the nuclear spins act as ‘quantum bits’¹⁹. The nuclear spins are particularly suited to this role because of their natural isolation from the environment. Our simple quantum computer solves a purely mathematical problem in fewer steps than is possible classically, requiring fewer ‘function calls’ than a classical computer to determine the global properties of an unknown function.

We implemented the simplest possible version of the Deutsch–Jozsa (D–J) quantum algorithm⁶, which determines whether an unknown function is constant or balanced. A constant function $f(x)$ that transforms N bits of information to one bit either has output $f(x) = 0$ for all x , or $f(x) = 1$ for all x . A balanced function has $f(x) = 0$ for exactly half of its inputs, and $f(x) = 1$ for the remaining inputs. To determine with certainty whether a function is constant or balanced on a deterministic classical computer requires up to $2^{N-1} + 1$ function calls: even if half of the inputs have been examined and $f(x) = 0$ has been found for each, it cannot be concluded with certainty that the function is constant. In contrast, the D–J algorithm, as improved by Cleve *et al.*²⁰ and by A. Tapp (personal communication), allows a quantum computer to determine whether $f(x)$ is constant or balanced using only one function call.

The D–J algorithm is well illustrated by its simplest possible case, when f is a function from one bit to one bit; this is the version that we have realized (it is also the simplest instance of Simon’s algorithm⁷). There are four possible functions f , two of which are constant, $f_1(x) = 0$, $f_2(x) = 1$, and two of which have an equal number of 0 and 1 outputs: $f_3(x) = x$, $f_4(x) = \text{NOT } x$. To determine whether such a function is constant or balanced is analogous to determining whether a coin is fair (with a head on one side and a tail on the other) or fake (heads on both sides). Classically, the coin is examined twice, first on one side then on the other, to determine whether it is fair or fake. The D–J algorithm exploits quantum coherence to determine whether a quantum ‘coin’ is fair or fake while looking at it only once. The algorithm requires one ‘input’ spin and one ‘work’ spin, and is schematically represented by the quantum circuit shown in Fig. 1.

Experimentally, this quantum algorithm was implemented using the nuclear spins of the ¹H and ¹³C atoms in a carbon-13 labelled chloroform molecule (CHCl₃) as the input and work quantum bits (‘qubits’). $|0\rangle$ ($|1\rangle$) describes the spin state aligned with (against)

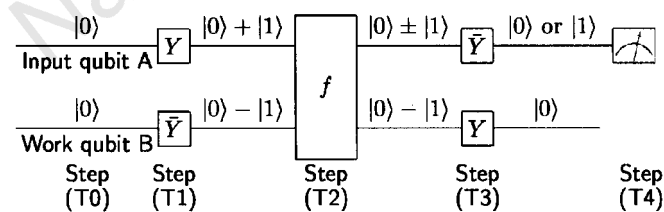


Figure 1 Quantum circuit for performing the D–J algorithm. T0, start with both the ‘input’ and ‘work’ qubits (A and B) in the state $|0\rangle$; T1, perform the transformation $Y : |0\rangle \rightarrow (|0\rangle + |1\rangle)/\sqrt{2}$, $|1\rangle \rightarrow (-|0\rangle + |1\rangle)/\sqrt{2}$, to A, and the inverse transformation \bar{Y} to B, resulting in the state $\frac{1}{2}\sum_{x=0}^1 |x\rangle (|0\rangle - |1\rangle)$. The input qubit in some quantum sense registers both 0 and 1 at once. T2, call the function: apply f to A, and add the result to B modulo 2. As long as the quantum logic operations needed to evaluate f are carried out coherently, the work qubit now contains in some quantum sense the outputs of f on all possible inputs, an effect that Deutsch termed ‘quantum parallelism’. The two qubits are now in the state $\frac{1}{2}\sum_{x=0}^1 |x\rangle (|0 + f(x)\rangle - |1 + f(x)\rangle) = \frac{1}{2}\sum_{x=0}^1 (-1)^{f(x)} |x\rangle (|0\rangle - |1\rangle)$. T3, perform the inverse of the transformations of (T1), thereby taking the qubits out of their superposition states. If f is constant, then the factors $(-1)^{f(x)}$ are either all +1 or all –1, and the result of the transformation in this step is the state $\pm |00\rangle$. If f is balanced, then exactly half of the factors $(-1)^{f(x)}$ are +1 and half are –1, and the result of the transformation is the state $\pm |10\rangle$. T4, read out A. If it is 0, then f is constant; if it is 1, then f is balanced.

an externally applied, strong static magnetic field \mathbf{B}_0 in the $+\hat{z}$ direction. The reduced hamiltonian for this 2-spin system is to an excellent approximation given by ($\hbar=1$)²¹: $\hat{\mathcal{H}} = -\omega_A \hat{I}_{zA} - \omega_B \hat{I}_{zB} + 2\pi J \hat{I}_{zA} \hat{I}_{zB} + \hat{\mathcal{H}}_{\text{env}}$. The first two terms describe the free precession of spin A (¹H) and B (¹³C) about $-\mathbf{B}_0$ with frequencies $\omega_A/2\pi \approx 500$ MHz and $\omega_B/2\pi \approx 125$ MHz. \hat{I}_{zA} is the angular momentum operator in the $+\hat{z}$ direction for A. The third term describes a scalar spin–spin coupling of the two spins of $J \approx 215$ Hz. $\hat{\mathcal{H}}_{\text{env}}$ represents coupling to the environment, including interactions with the chlorine nuclei, and also higher order terms in the spin–spin coupling, which can be disregarded (as will be described below).

The five theoretical steps of the quantum algorithm, (T0)–(T4), were experimentally implemented as follows.

E0. An initial state is prepared with a 200 mM, 0.5 ml sample of chloroform dissolved in *d*6-acetone, at room temperature and standard pressure. The $O(10^{18})$ molecules in this bulk sample can be thought of as being independent single quantum computers, all functioning simultaneously. The theoretically ideal result is obtained when the spins in all the molecules start out in the 00 state—that is, all spins aligned in the $+\hat{z}$ direction. Because the experiment is performed at room temperature, however, the initial density matrix ρ for the thermally equilibrated system has populations $\text{diag}(\rho) = [n_{00}, n_{01}, n_{10}, n_{11}]$ in the 00, 01, 10 and 11 states, respectively, where ρ is the density matrix, and n_i are proportional to $e^{-E_i/kT}/2^N \approx (1 - E_i/kT)/2^N$, with E_i the energy of state i , and $N = 2$ the number of qubits used in our experiment. A variety of techniques exist to extract from this thermal state just the signal from the molecules in the 00 state^{16,17}; we adopted the method of ‘temporal averaging’²², which involves the summation of three experiments in which the populations of the 01, 10 and 11 states are cyclically permuted before performing the computation. The essential observation is that $[n_{00}, n_{01}, n_{10}, n_{11}] + [n_{00}, n_{11}, n_{01}, n_{10}] + [n_{00}, n_{10}, n_{11}, n_{01}] = \alpha[1, 1, 1, 1] + \delta[1, 0, 0, 0]$, where $\alpha = n_{01} + n_{10} + n_{11}$ is a background signal which is not detected, and $\delta = 3n_{00} - \alpha$ is a deviation from the uniform background whose signal behaves effectively like the desired pure quantum state, $|00\rangle$. The permutations are performed using methods similar to those used for the computation, described next. This technique avoids the technical difficulties of detecting the signal from a single nuclear spin, and allows a sample at room temperature, which produces an easily detectable signal, to be used for quantum computation.

Note that although this method requires $f(x)$ to be evaluated three times, it is actually not necessary. Although step (T0) stipulates a pure initial state $|00\rangle$, the algorithm works equally well if the input qubit is initially $|1\rangle$; furthermore, when the work qubit is initially $|1\rangle$, it fails, and cannot distinguish constant from balanced functions, but this does not interfere with other computers which have worked. Thus, a thermal state is a good initial state for this algorithm, and only one experiment needs to be done. Data from both thermal and pure state inputs are presented below.

E1. Pulsed radiofrequency electromagnetic fields are applied to transform the qubits as prescribed in (T1). These fields, oriented in the $\hat{x} - \hat{y}$ plane perpendicular to \mathbf{B}_0 , selectively address either A or B by oscillating at frequency ω_A or ω_B . Classically, a radiofrequency pulse along \hat{y} (for example) rotates a spin about that axis by an angle proportional to $\sim tP$, the product of the pulse duration t and pulse power P . In the ‘bar magnet’ picture, a $\pi/2$ pulse along \hat{y} (we shall call this Y) causes a \hat{z} oriented spin to be rotated by 90° , onto \hat{x} (similarly, we shall let \bar{Y} denote $\pi/2$ rotations about $-\hat{y}$, and X denote $\pi/2$ rotations about \hat{x} , and so forth; subscripts will identify which spin the operation acts upon). This description of the state is classical in the sense that a bar magnet always has a definite direction. In reality, however, a nuclear spin is a quantum object, and instead of being aligned along \hat{x} , it is actually in a superposition of being up and down, $(|0\rangle + |1\rangle)/\sqrt{2}$. Likewise, a spin classically

described as being along $-\hat{x}$ is actually in the state $(|0\rangle - |1\rangle)/\sqrt{2}$. (E1) thus consists of applying the two radiofrequency pulses $Y_A Y_B$. E2. The function $y \rightarrow y \oplus f(x)$ is implemented using radiofrequency pulses and spin-spin interaction. Recall that spin A represents the input qubit x , and B the work qubit y where f stores its output. f_1 is implemented as $\tau/2 - X_B X_B - \tau/2 - X_B X_B$, to be read from left to right, where $\tau/2$ represents a time interval of $1/4J \approx 1.163$ ms, during which coupled spin evolution occurs. Dashes are for readability only, and typical pulse lengths were 10–15 μ s. This is a well known refocusing²³ pulse sequence which performs the identity operation. f_2 is $\tau/2 - X_B X_B - \tau/2$, similar to f_1 but without the final pulses, so that B is inverted. f_3 is $Y_B - \tau - \bar{Y}_B X_B - \bar{Y}_A \bar{X}_A Y_A$, which implements a ‘controlled-NOT’ operation, in which B is inverted if, and only if, A is in the $|1\rangle$ state. The naive ‘bar magnet’ picture can be used to get a feeling for how this works in case the inputs are 00 or 10, for which the subsequence $Y_B - \tau - X_B$ suffices (note that after (E1), both spins are not just $|0\rangle$ or $|1\rangle$ but in a superposition of both, in which case the extra pulses of f_3 are necessary¹⁶). First, Y_B rotates B to $+\hat{x}$. B then precesses in the $\hat{x} - \hat{y}$ plane, about $-\hat{z}$. Owing to the spin-spin coupling, B precesses slightly slower (faster) if $A = 0$ ($A = 1$). After τ seconds, B reaches $+\hat{y}$ ($-\hat{y}$) in the rotating frame. X_B then rotates B to $+\hat{z}$ ($-\hat{z}$), that is, to 0 or 1, where the final state of B depends on the input A. The precise quantum description is easily obtained by multiplying out the

unitary rotation matrices. Finally, f_4 is implemented as $Y_B - \tau - \bar{Y}_B \bar{X}_B - \bar{Y}_A \bar{X}_A Y_A$, which is similar to f_3 but leaves B inverted. E3. The inverse of (E1) is done by applying the radiofrequency pulses $\bar{Y}_A Y_B$ to take both spins back to $\pm\hat{z}$. Spin A, which was $|0\rangle$ at the input, is thus transformed into $|0\rangle$ or $|1\rangle$ for constant or balanced functions respectively. E4. The result is read out by applying a read-out pulse X_A to bring spin A back into the $\hat{x} - \hat{y}$ plane. The time varying voltage $V(t)$ induced by the precession of spin A about $-\mathbf{B}_0$ is recorded by a phase sensitive pick-up coil. Inspection of the spectrum of $V(t)$ after a single experiment run and an appropriate read-out pulse, immediately reveals whether $f(x)$ is constant or balanced (Fig. 2).

We also characterized the entire deviation density matrix $\rho_\Delta \equiv \rho - \text{Tr}(\rho)I/4$ (Fig. 3) describing the final 2-qubit state. These results unambiguously demonstrate the complete proper functioning of the quantum algorithm, and provide data for the error analysis described below.

Quantum computation requires that a coherent superposition be preserved for the duration of the computation. This requires a highly isolated quantum system (small \mathcal{H}_{env}), and fortunately, nuclear spins are naturally well isolated from their environment. Phase randomization due to \mathbf{B}_0 inhomogeneities was minimized by using about 30 electromagnetic coils to shim the static field to be constant to about one part in 10^9 over the sample volume. The

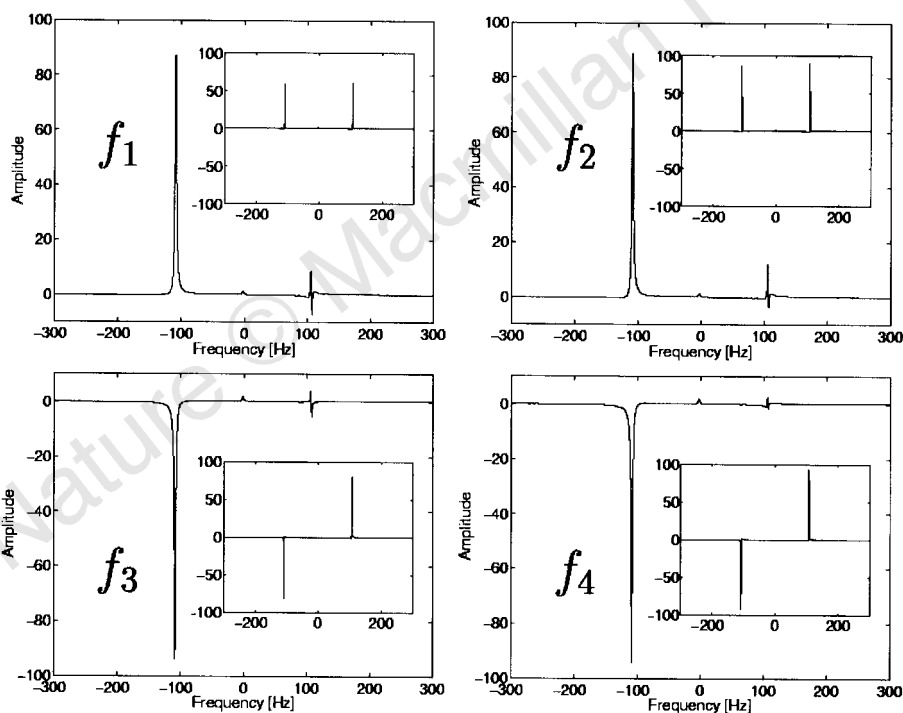


Figure 2 Proton spectrum after completion of the D-J algorithm and a single read-out pulse X_A , with an effectively pure initial state $|00\rangle$ and with a thermal initial state (inset). The low/high-frequency lines correspond to the transitions $|00\rangle \leftrightarrow |10\rangle$ ($|01\rangle \leftrightarrow |11\rangle$). The frequency is relative to 499,755,169 Hz, and the amplitude has arbitrary units. The spectrum is the Fourier-transformed time varying voltage $V(t)$, induced in the pick up coil by the precession of spin A about $-\mathbf{B}_0$, at frequency ω_A , after the read-out pulse X_A . $V(t)$ is given by $V(t) \approx V_0 \text{Tr}[e^{-i\omega_A t} e^{-i(\pi/2)\hat{y}_x} \rho(0) e^{i(\pi/2)\hat{y}_x} e^{i\omega_A t} \times (-i\sigma_{xA} - \sigma_{yA})]$, where $\sigma_{(xy)}$ are Pauli matrices, and $\rho(0)$ is the density matrix of the state immediately before the readout pulse. By this convention, a spectral line for spin A is real and positive (negative) when spin A is $|0\rangle$ ($|1\rangle$) right before the X_A read-out pulse. Experiments were performed at Stanford University using an 11.7-Tesla Oxford Instruments magnet and a Varian^{UNIVERSITY} Inova spectrometer with a triple-resonance probe. ¹³C-labelled CHCl_3 was obtained from Cambridge Isotope Laboratories.

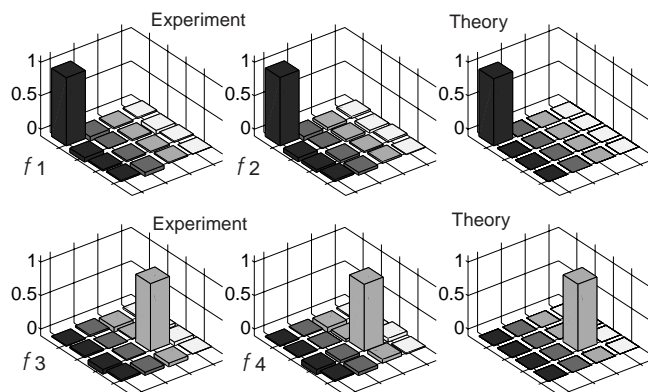


Figure 3 Experimentally measured and theoretically expected deviation density matrices after completion of the D-J algorithm. The diagonal elements represent the normalized populations of the states $|00\rangle$, $|01\rangle$, $|10\rangle$ and $|11\rangle$ (from left to right). The off-diagonal elements represent coherences between different states. The magnitudes are shown with the sign of the real component; all imaginary components were small. The deviation density matrix was obtained from the integrals of the proton and carbon spectral lines, acquired for a series of 9 experiments with different read-out pulses for each spin (quantum state tomography²⁴). The observed experimental non-idealities can be quantified as follows. In the experiments, the normalized pure-state population (ideally equal to 1), varied from 0.998 to 1.019. The other deviation density matrix elements (ideally 0), were smaller than 0.075 in magnitude. The relative error ϵ on the experimental pure-state output density matrix ρ_{exp} , defined as $\epsilon = \|\rho_{\text{exp}} - \rho_{\text{theory}}\| / \|\rho_{\text{theory}}\|$, varied between 8 and 12%.

longitudinal and transverse relaxation time constants T_1 and T_2 were measured using standard inversion–recovery and Carr–Purcell–Meiboom–Gill pulse sequences²³, giving $T_1 \approx 19$ and 25 s, and $T_2 \approx 7$ and 0.3 s, respectively, for proton and carbon; these were much longer than required for our experiment, which finished in about 7 ms.

The single most important source of errors in the experiments was the radiofrequency field inhomogeneity and pulse-length calibration imperfections. A direct measure of this inhomogeneity is the ~ 200 - μ s time constant of the exponentially decaying envelope observed from applying a single pulse as a function of pulse length. Including the population permutation sequence, about 7 pulses are applied to each nucleus, with a cumulative duration of ~ 70 – 100 μ s.

The second most important contribution to errors is the low carbon signal-to-noise ratio, signal peak height/r.m.s. noise ≈ 35 , versus about 4,300 for proton. The carbon signal was much weaker because the carbon gyromagnetic ratio is 4 times smaller, and the carbon receiver coil is mounted more remotely from the sample. Smaller contributions to errors came from incomplete relaxation between subsequent experiments, carrier frequency offsets and numerical errors in the data analysis.

For this small-scale quantum computer, imperfections were dominated by technology, rather than by fundamental issues. However, NMR quantum computers larger than about 10 qubits will require creative new approaches, because the signal strength decays exponentially with the number of qubits in the machine, using current schemes^{24,25}: for N spins, the signal from the initial state $00\dots 0$ is proportional to $n_{00\dots 0} \propto NZ^{-N}$, where the single spin partition function $Z \approx 2$ at high temperatures. Furthermore, coherence times typically decrease for larger molecules, whereas the average logic gate duration increases. Nevertheless, there is hope; for example, because of the ensemble nature of the NMR approach, the output result can be inferred as long as a distinguishable majority of the molecules reach the correct final state. Creating an effective pure state is thus not always necessary, as we have demonstrated. Optical pumping and other cooling techniques can also be used to prepolarize the sample to increase the output signal amplitude, because $Z \approx 1$ at low temperatures. Quantum computation poses an interesting and relevant experimental challenge for the future.

Note added in proof: During the course of this work, we became aware of a closely related experiment by J. A. Jones and M. Mosca²⁶.

Received 21 January; accepted 18 March 1998.

1. Deutsch, D. Quantum theory, the Church-Turing principle and the universal quantum computer. *Proc. R. Soc. Lond. A* **400**, 97–117 (1985).
2. Shor, P. Algorithms for quantum computation: discrete logarithms and factoring. *Proc. 35th Annu. Symp. on Found. of Computer Science* 124–134 (IEEE Comp. Soc. Press, Los Alamitos, CA, 1994).
3. Divincenzo, D. P. Quantum computation. *Science* **270**, 255–261 (1995).
4. Lloyd, S. Quantum-mechanical computers. *Sci. Am.* **273**, 44–50 (1995).
5. Ekert, A. & Jozsa, R. Quantum computation and Shor's factoring algorithm. *Rev. Mod. Phys.* **68**, 733–753 (1996).
6. Deutsch, D. & Jozsa, R. Rapid solution of problems by quantum computation. *Proc. R. Soc. Lond. A* **439**, 553–558 (1992).
7. Simon, D. On the power of quantum computation. *Proc. 35th Annu. Symp. on Found. of Computer Science* 116–124 (IEEE Comp. Soc. Press, Los Alamitos, CA, 1994).
8. Grover, L. K. Quantum computers can search arbitrarily large databases by a single query. *Phys. Rev. Lett.* **79**, 4709–4712 (1997).
9. Urruh, W. G. Maintaining coherence in quantum computers. *Phys. Rev. A* **51**, 2, 992–997 (1995).
10. Chuang, I. L., Laflamme, R., Shor, P. & Zurek, W. H. Quantum computers, factoring, and decoherence. *Science* **270**, 1633–1635 (1995).
11. Landauer, R. Dissipation and noise immunity in computation and communication. *Nature* **335**, 779–784 (1988).
12. Landauer, R. Is quantum mechanics useful? *Phil. Trans. R. Soc. Lond. A* **335**, 367–376 (1995).
13. Palma, G. M., Suominen, K.-A. & Ekert, A. K. Quantum computers and dissipation. *Proc. R. Soc. Lond. A* **452**, 567–584 (1996).
14. Monroe, C., Meekhof, D. M., King, B. E., Itano, W. M. & Wineland, D. J. Demonstration of a fundamental quantum logic gate. *Phys. Rev. Lett.* **75**, 4714–4717 (1995).
15. Turchette, Q. A., Hood, C. J., Lange, W., Mabuchi, H. & Kimble, H. J. Measurement of conditional phase shifts for quantum logic. *Phys. Rev. Lett.* **75**, 4710–4713 (1995).
16. Gershenfeld, N. & Chuang, I. L. Bulk spin-resonance quantum computation. *Science* **275**, 350–356 (1997).
17. Cory, D. G., Price, M. D., Fahmy, A. F. & Havel, T. F. Nuclear magnetic resonance spectroscopy: an experimentally accessible paradigm for quantum computing. *Physica D* (in the press; LANL E-print quant-ph/9709001.gov, 1997).

18. Cory, D. G., Fahmy, A. F. & Havel, T. F. Ensemble quantum computing by NMR spectroscopy. *Proc. Natl Acad. Sci. USA* **94**, 1634–1639 (1997).
19. Lloyd, S. A potentially realizable quantum computer. *Science* **261**, 1569–1571 (1993).
20. Cleve, R., Ekert, A., Macchiavello, C. & Mosca, M. *Proc. R. Soc. Lond. A* **454**, 339–354 (1998). LANL E-print quant-ph/9708016.
21. Slichter, C. P. *Principles of Magnetic Resonance* (Springer, Berlin, 1990).
22. Knill, E., Chuang, I. L. & Laflamme, R. Effective pure states for bulk quantum computation. *Phys. Rev. A* **57**(5), May (1998).
23. Ernst, R. R., Bodenhausen, G. & Wokaun, A. *Principles of Nuclear Magnetic Resonance in One and Two Dimensions* (Oxford Univ. Press, Oxford, 1994).
24. Chuang, I. L., Gershenfeld, N., Kubinec, M. G. & Leung, D. W. Bulk quantum computation with nuclear magnetic resonance: Theory and experiment. *Proc. R. Soc. Lond. A* **454**, 447–467 (1998).
25. Warren, W. S. The usefulness of NMR quantum computing. *Science* **277**, 1688–1690 (1997).
26. Jones, T. F. & Mosca, M. Implementation of a quantum algorithm to solve Deutsch's problem on a nuclear magnetic resonance quantum computer. *J. Chem. Phys.* (in the press; LANL E-print quant-ph/9801027).

Acknowledgements. We thank A. Pines and M. Kubinec for discussion. This work was supported by DARPA under the NMRQC and QUIC initiatives. L.V. gratefully acknowledges a Francqui Fellowship of the Belgian American Educational Foundation and a Yansouni Family Fellowship.

Correspondence and requests for materials should be addressed to I.L. (e-mail: ichuang@almaden.ibm.com).

Spontaneous formation of ordered structures in thin films of metals supported on an elastomeric polymer

Ned Bowden*, Scott Brittain*, Anthony G. Evans†, John W. Hutchinson† & George M. Whitesides*

* Department of Chemistry and Chemical Biology, Harvard University, 12 Oxford Street, Cambridge, Massachusetts 02138, USA

† Department of Engineering and Applied Sciences, Harvard University, Pierce Hall, Cambridge, Massachusetts 02138, USA

Spontaneous generation of complex order in apparently simple systems is both arresting and potentially useful^{1–11}. Here we describe the appearance of complex, ordered structures induced by the buckling of thin metal films owing to thermal contraction of an underlying substrate. We deposit the films from the vapour phase on a thermally expanded polymer (polydimethylsiloxane, PDMS). Subsequent cooling of the polymer creates compressive stress in the metal film that is relieved by buckling with a uniform wavelength of 20–50 micrometres. The waves can be controlled and orientated by relief structures in the surface of the polymer, which can set up intricate, ordered patterns over large areas. We can account qualitatively for the size and form of the patterned features in terms of the non-uniform stresses developed in the film near steps on the polymer substrate. This patterning process may find applications in optical devices such as diffraction gratings and optical sensors, and as the basis for methods of strain analysis in materials.

Thin metal films—typically 50-nm-thick layers of gold with a 5-nm adhesion interlayer of titanium or chromium—were deposited onto PDMS by electron beam evaporation (Fig. 1). The metal source heats and expands the PDMS substrate before and during deposition. We believe that local heating of the surface of the PDMS also slightly modifies its mechanical properties; perhaps by introducing new crosslinks¹². After cooling to ambient temperature, the surface appeared frosted, because of light scattering from a network of periodic surface waves (Fig. 2a)¹³. Similar waves were found with a variety of metals, including nickel, aluminum, titanium and chromium. The waves almost disappeared when the sample was reheated to 110 °C, but reformed on cooling. They also formed on PDMS externally heated to 300 °C during the evaporation of metal. Conversely, when the PDMS was cooled to 0 °C during evaporation of metal, waves did not arise; this observation verifies the central importance of the thermal excur-